PSFC/JA-06-34

Identification of TEM Turbulence through Direct Comparison of Nonlinear Gyrokinetic Simulations with Phase Contrast Imaging Density Fluctuation Measurements

D.R. Ernst, N. Basse, W. Dorland[1], C.L. Fiore, L. Lin, A. Long[2], M. Porkolab, K. Zeller, K. Zhurovich

June 2006

Plasma Science and Fusion Center
Massachusetts Institute of Technology
Cambridge MA 02139 USA

[1]Physics Department, Univ. of Maryland, College Park, MD, USA
[2]Physics Departmetnt, Cornell University, Ithaca, NY, USA

Submitted for publication to *Nuclear Fusion.*

Identification of TEM Turbulence through Direct Comparison of Nonlinear Gyrokinetic Simulations with Phase Contrast Imaging Density Fluctuation Measurements

D. R. Ernst 1), N. Basse 1), W. Dorland 2), C. L. Fiore 1), L. Lin 1), A. Long 3), M. Porkolab 1), K. Zeller 1), and K. Zhurovich 1)

1) Plasma Science and Fusion Center, Mass. Inst. of Technology, Cambridge, MA, USA
2) Physics Department, Univ. of Maryland, College Park, MD, USA
3) Physics Department, Cornell University, Ithaca, NY, USA

e-mail contact of main author: dernst@psfc.mit.edu

Abstract. Nonlinear gyrokinetic simulations of Trapped Electron Mode (TEM) turbulence have reproduced measured particle fluxes and thermal energy fluxes, within experimental uncertainty, in Alcator C-Mod [1, 2]. This has provided a model for internal transport barrier control with on-axis ICRH in Alcator C-Mod, without adjustable model parameters. The onset of TEM turbulent transport limits the density gradient, preventing radiative collapse. Here we move beyond comparisons of simulated and measured fluxes to a more fundamental and direct comparison with density fluctuation spectra. Using a new synthetic diagnostic, excellent agreement is obtained between wavelength spectra from nonlinear GS2 simulations, and spectra measured by Phase Contrast Imaging. The density fluctuations are associated with the steep density gradient in the C-Mod ITB, which provides spatial localization for the chordal PCI measurement. Gyrokinetic stability analysis shows that Trapped Electron Modes are strongly destabilized inside the ITB foot by the addition of on-axis ICRH. Nonlinear GS2 simulations reproduce the relative increase in fluctuation level when on-axis heating is applied. Further, we have extended the GS2 Lorentz collision operator to include classical diffusion associated with the ion finite Larmor radius, and have implemented collisional energy diffusion, together with particle, momentum, and energy conservation terms. Classical diffusion is shown to strongly stabilize trapped electron modes with $k_\theta \rho_i > 2$ for realistic C-Mod collisionalities. A series of detailed nonlinear gyrokinetic simulations show the nonlinear upshift [1, 2] in the TEM critical density gradient increases favorably with collisionality.

1. Introduction

Trapped electron mode turbulence is relevant to particle and electron thermal energy transport. Several types of TEM exist, driven by either the electron density gradient, or by the electron temperature gradient. The most significant modes are associated with non-resonant "bad curvature" drive as well as toroidal precession drift resonance. TEM turbulence is most relevant when toroidal ITG modes are either stable or weakly unstable. This scenario arises in a variety of contexts, such as internal transport barriers, cases with strong density peaking, cases with $T_e > T_i$, and low density regimes in which confinement scales favorably with density. Understanding of the mechanisms underlying particle and electron thermal energy transport could impact future devices such as ITER,
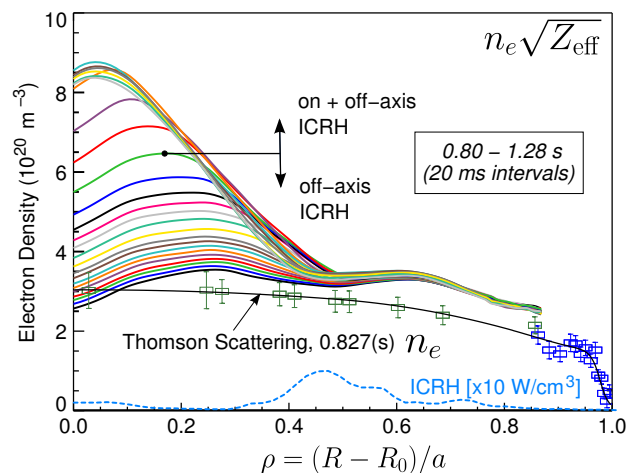

FIG. 1. Density profile evolution in the C-Mod ITB, from CCD based visible Bremsstrahlung.

where core fueling is greatly reduced, and electrons are heated directly by α-particles. In the Alcator C-Mod cases studied, TEM turbulence produces strong particle and electron thermal energy transport as the density gradient, and the electron temperature, increase. This mechanism provides a model for the observed control [3, 4, 5, 6] of the density profile in the C-Mod ITB using on-axis ICRH. In earlier efforts, radial and poloidal wavelength spectra from gyrokinetic particle simulations of ITG turbulence, with adiabatic electrons [7], were observed to resemble density fluctuations in TFTR [8], as measured by localized Beam Emission Spectroscopy. Recent gyrokinetic simulations of ITG turbulence have attained sufficient realism to reproduce experimental heat fluxes [9], but comparisons with between nonlinear simulations and fluctuation measurements have not been forthcoming. Similarly, nonlinear gyrokinetic simulations of pure TEM turbulence have just begun, for the density gradient driven [1, 2] and temperature gradient driven [10, 11] cases.

2. Experimental Scenario

The C-Mod ITB provides a unique opportunity in two respects. First, the strong fluctuations in the ITB, driven by the strong density gradient, allow spatial localization of the chordal phase contrast imaging density fluctuation measurement. Second, without core particle fueling, ITER like densities, and $\sim$1 mm between density spatial channels, the C-Mod experiments provide an excellent test bed for particle transport studies. This study focuses on a case in which the full available ICRH source power ($\sim$4 MW) was injected both off-axis, near the half-radius (2.3 MW), and on-axis (1.6 MW), to maintain the C-Mod ITB. Off-axis heating is used to first establish EDA H-Mode, an ELM-free, quiescent regime with steady pedestal density, which is regulated by the Quasi Coherent (QC) mode in the pedestal [12]. The ITB forms during 25-30 energy confinement times as a result of the Ware pinch [13], with ITG turbulence suppressed by off-axis heating, which broadens the temperature profile. The electron density profiles at 20 ms intervals are shown in Fig. 1, as a function of $\rho \sim r/a$, the normalized square root of toroidal flux. The CCD based visible Bremsstrahlung emission profiles are acquired with sub-ms sampling and $\sim$1 mm channel spacing [14]. Thomson scattering data for the early EDA H-Mode phase is also shown. The profile of $n_e Z_{eff}^{1/2}$, hereafter referred to as the density profile, attains a quasi-steady value shortly after on-axis ICRH is applied at 1.10 seconds, as shown in Fig. 2. The on-axis ICRH produces
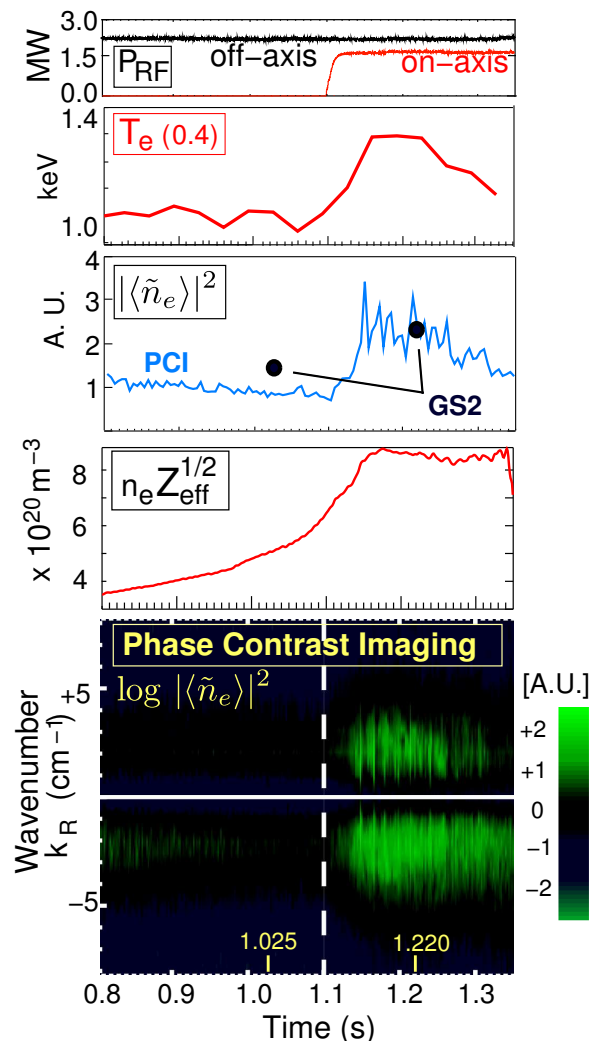

FIG. 2. Injected power, T_e in ITB, PCI fluctuation power from chord 12 with GS2 nonlinear simulations before/during on-axis ICRH (normalized at 1.22 s), maximum electron density, and log of PCI autopower spectrum (20-80 kHz) vs. k_R and time.
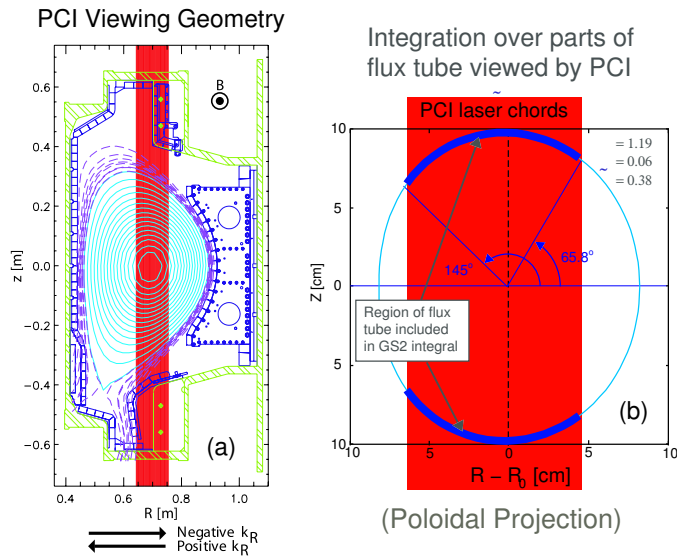
FIG. 3. (a) 32 PCI laser chords, and (b) integration domain for synthetic PCI in GS2.
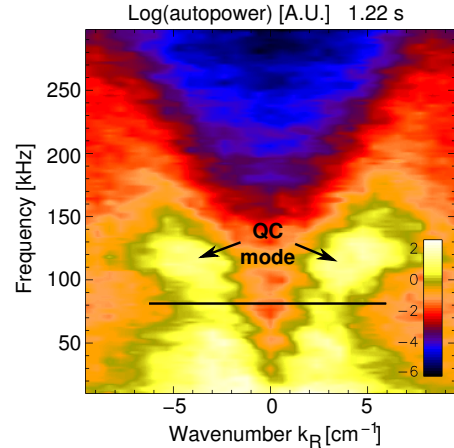

FIG. 4. Autopower spectrum from PCI at 1.22 sec., showing quasi-coherent mode is well-separated from the low frequency turbulence of interest.

a 30% increase in electron temperature in the ITB, as shown in Fig. 2. The PCI wavenumber spectrum, integrated over the frequency range 20-80 kHz, is also shown as a function of time in Fig. 2. Strong density fluctuations appear in the range $1 < k_R < 5$ cm^{-1} during on-axis heating. The 32 vertical PCI [15] laser chords are shown in Fig. 3(a). The laser beams pass through a phase plate and interfere with a reference beam on a detector array. The radius of a laser spot on the detector is proportional to the scattering wavenumber, and its azimuthal location is perpendicular to the magnetic field, for field-aligned fluctuations. The spectrum as a function of wavenumber in the major radius direction is obtained using the 32 channels. A wider freqency range is shown in Fig. 4 at 1.22 seconds, during on-axis heating. The edge quasi-coherent mode, above 80 kHz, is separated from the low freqency turbulence of interest. In wavelength spectra to follow, we have removed the QC mode frequencies using a notch filter, followed by an exponential fit in frequency. The wavelength spectra resulting from integration over 20-80 kHz, 10-80 kHz, or the entire frequency range (filtering the QC mode), are nearly identical. For this 2004 discharge, the PCI system had 13 cm coverage in major radius, 10 MHz sampling, and a wavenumber range extending to ± 8.3 cm^{-1}, using a 25 W CO_2 laser with 10.6 μm wavelength. Recent upgrades have increased the laser power to 60 W, the wavelength range to ± 40 cm^{-1}, a new phase plate mask has differentiated top and bottom QC mode spectra, and a new absolute calibration system has been developed.

3. Gyrokinetic Turbulence Simulations and Comparison with Fluctuation Data

To explore the origin of the strong density fluctuations observed during on-axis heating, we consider two times for analysis, before on-axis heating (1.025 s) and during on-axis heating (1.220 s). We first carry out linear gyrokinetic stability analysis using the GS2 code [16, 17], in conjunction with automated data preparation and analysis tools [18]. We have recently developed a graphical profile fitting tool fiTS for C-Mod temperature and density profile data (sample profiles are shown in Fig. 1 and Fig. 5(c)). TRANSP analysis provides the consistent magnetic equilibrium and profile data for GS2. At each radius, $k_\theta \rho_i$ is scanned over the range 0 to 2 to determine the maximum linear growth rate. Classical diffusion, described in Sec. 4., is included for all points, effectively limiting the unstable range of wavelengths. Prior to on-axis heating, toroidal ITG modes are dominant inside the ITB, and TEMs are stable, as shown in Fig. 5(a). Here all positive growth rates are ITG modes unless otherwise indicated. In

Fig. 5(d), the main effect of the on-axis ICRH is to increase the temperature by ∼30% inside the ITB foot. At the same time, the region over which the driving factor for the TEM, the inverse density gradient scale length, is large, expands. This combination of factors strongly destabilizes TEMs inside the ITB, indicated by the shaded region in Fig. 5(a). The $Z_{\rm eff}$ gradient scale length is the most significant source of uncertainty in this calculation [1]. In principle, the $Z_{\rm eff}$ profile can be obtained from the square of the ratio of visible Bremsstrahlung and Thomson scattering data, but with ±50% statistical error. Further, with effectively three channels inside the ITB foot, Thomson scattering, which is calibrated to ECE cutoff at lower densities, does not yield reliable ITB density gradients for this case. Here we have assumed a flat $Z_{\rm eff}$ profile, and taken the density gradient scale length from the visible Bremsstrahlung array. Stability analysis using Thomson scattering density profiles and inferred $Z_{\rm eff}$ profiles yields the same qualitative result – that TEMs are driven unstable inside the ITB during on-axis ICRH, with a very similar growth rate profile.

Density fluctuations from a sample nonlinear GS2 simulation at 1.22 seconds, ρ = 0.4, are shown in Fig. 6. The simulation shown required over 24 hours on 2640 processors on an IBM SP Power 3 system (NERSC). Another simulation was carried out for the same radius at time 1.025 seconds. An initial comparison with PCI chordal fluctuation data, without the synthetic diagnostic, is shown in Fig. 2(c). The nonlinear simulations appear to reproduce the measured relative increase in density fluctuation level, with the application of on-axis ICRH.
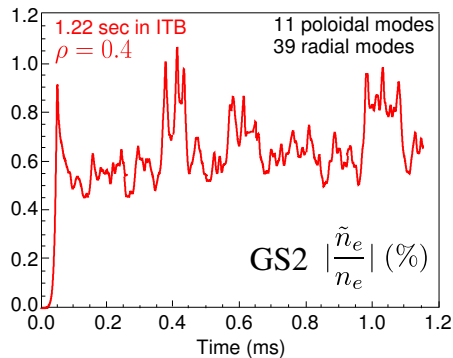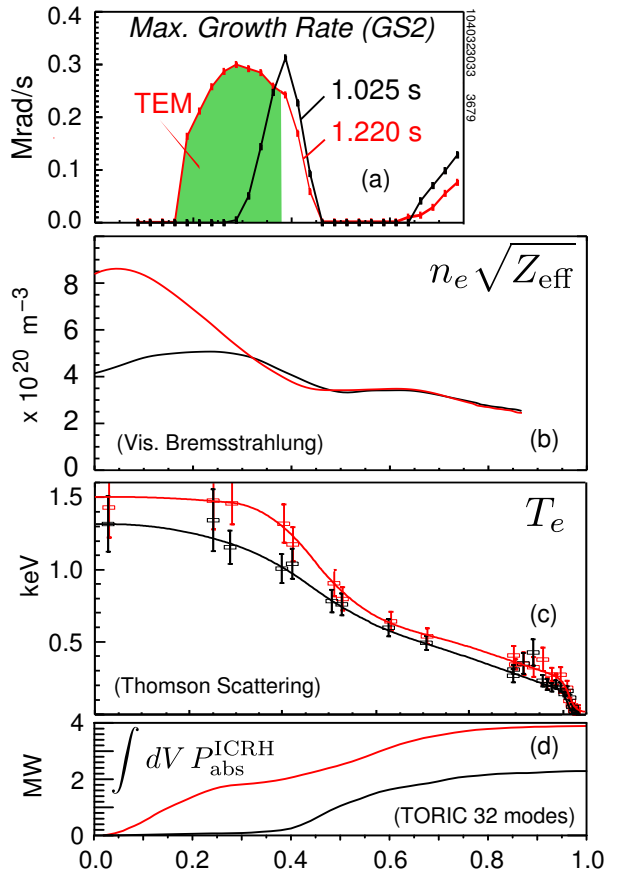

FIG. 5. *(a) Growth rate profiles before and during on-axis ICRH, (b) Electron density profiles, (c) Electron temperature profiles, and (d) volume integrated ICRH power absorbed from TRANSP (TORIC).*

FIG. 6. *Density fluctuations from nonlinear GS2 simulation at 1.22 s, during on-axis heating.*

To provide a direct comparison with PCI fluctuation data, we developed a synthetic PCI diagnostic for GS2 [19]. The GS2 simulation domain is a field line following flux tube extending several toroidal transits, with a cross-section typically 60-100 ion gyro-radii in size (multiple radial correlation lengths) at the outboard midplane. The simulation domain deforms with magnetic shear. Clebsch coordinates (ψ, α, θ) are used, where ψ labels flux surfaces, $\alpha = \zeta - q\theta$ labels field lines, and θ is the poloidal projection of the coordinate parallel to the magnetic field. The synthetic diagnostic involves transforming from the flux-tube simulation's Clebsch coordinates to Cartesian coordinates, and integrating the density fluctuations over por-

tions of the flux tube viewed by PCI, as shown in Fig. 3(b). The coordinate transformation assumes a Miller equilibrium [20] to obtain the projection onto the PCI major radial wavevector, $k_R = (\nabla R \cdot \nabla \psi)/|\nabla \psi|)k_\psi + (\nabla R \cdot \nabla \alpha/|\nabla \alpha|)k_\alpha$, analytically. Because the the PCI radial coverage is wider than a single GS2 flux tube, we integrate along the flux tube over the region of the poloidal plane intersected by PCI laser chords. Because the flux tube is many correlation lengths wide, this is equivalent to making statistically independent copies of the flux tube and rotating each to form a contiguous series, covering the PCI region of the poloidal plane. Following this integration, we apply a PCI instrument function to the GS2 data. The instrument function accounts for the Gaussian laser beam profile, finite aperture effects, and reduced sensitivity near $k_R \simeq 0$. Fig. 7 shows excellent agreement between simulated and measured wavelength spectra of density fluctuations during on-axis heating. In conjunction with the gyrokinetic stability analysis, which shows the TEM is the only unstable mode in the ITB, this implies that the strong turbulent fluctuations observed are due to TEM turbulence.

The PCI chords cover a relative wide range of major radii for the flux surface of interest, and k_R is a linear combination of radial and poloidal wavenumbers. The radial k_ψ spectrum is dominated by zonal flows and tends to peak at $k_\psi = 0$, while the poloidal k_α spectrum tends to be downshifted from the linear growth rate spectrum. If PCI had negligible radial extent, it would view primarily poloidal wavenumbers, with $k_R \simeq -k_\theta$. The addition of the radial wavenumber spectrum in the synthetic diagnostic provides the downshift needed to produce agreement with PCI. Finally, in Fig. 7, the level of density fluctuations prior to on-axis heating is much lower, as would be consistent with the gyrokinetic stability analysis in Fig. 5, which suggests longer wavelength toroidal ITG turbulence in the presence of reduced heating power.
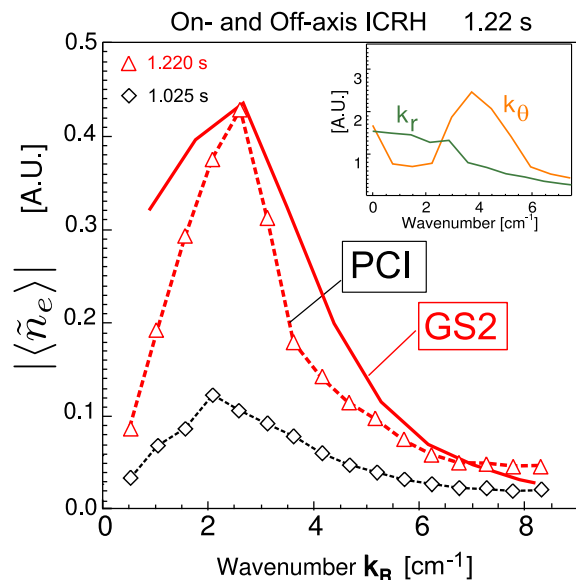

FIG. 7. *Comparison of spectra of density fluctuations from PCI, and from GS2 nonlinear simulation with synthetic PCI diagnostic. GS2 spectrum is linear combination of radial and poloidal wavenumber spectra shown in inset.*

4. Upgraded GS2 Collision Operator

The effect of classical ion diffusion, or Finite Larmor Radius collisional terms, on TEM stability was initially investigated [21], using a simplified local analysis. The linearized Lorentz collision operator was extended analytically to include FLR and energy diffusion terms [22], yielding a simple $O(k_\perp^2 \rho_i^2)$ correction. We have implemented the full FLR correction of Ref. [22] in GS2 as a Krook operator with particle and momentum conserving terms. The operator is applied following the usual GS2 Lorentz operator. The effect of this classical diffusion correction can be quite significant for TEMs, which tend to have shorter poloidal wavelengths, and tend to have eigenfunctions that are more extended along field lines. For a given toroidal mode number n, with $k_\theta = nq/r$, the relation $k_\perp^2 = k_\theta^2(1 + \hat{s}^2(\theta - \theta_0)^2)$ implies that large values of $k_\perp^2 \rho_i^2$ can be attained in the tails of the eigenfunction. Here $\hat{s}$ is the magnetic shear, and θ measures the distance along field lines. Accordingly, classical diffusion can have a strong damping effect on shorter wavelengths, as

shown in Fig. 8. Here the "Cyclone Base Case" [23] parameters are used, with the temperature gradient set to zero and the density gradient above the TEM threshold. Both cases are shown for a collisionality relevant to the C-Mod half-radius. Classical diffusion effectively damps all TEM with $k_\theta \rho_i > 2$, for the case of interest, eliminating the extended tail in the spectrum. All linear growth rate calculations presented in Sec. 3. were carried out with classical collisional diffusion included. A similar correction was separately implemented without conserving terms [24], but no physical effect was seen for microtearing modes.

We have also successfully implemented energy diffusion, with associated momentum and energy conserving terms, in the GS2 collision operator fully implicitly [25]. Significant parallel programming effort was required to create a local distribution contiguous in energy, and to redistribute results among processors. Physical effects of collisional energy diffusion will be reported elsewhere.

5. Nonlinear Upshift of TEM Critical Density Gradient

In Ref. [1, 2], the existence of a nonlinear upshift in the TEM critical density gradient was observed, analogous to the Dimits shift in the critical temperature gradient for ITG turbulence. We have carried out over one hundred detailed nonlinear gyrokinetic simulations of

FIG. 8. *Effect of ion classical diffusion on TEM linear growth rate spectrum, for collisionality relevant to C-Mod half-radius. Cyclone base case parameters, zero temperature gradient.*

TEM turbulence to investigate the parametric dependence of the upshift [26]. This study uses Cyclone Base Case parameters, but with zero temperature gradient, varying the density gradient and collisionality, while maintaining consistent ion and electron collision frequencies. Near the linear critical density gradient, in the upshift regime, zonal flow dominated states arise, as shown in Fig. 9(a,b). A single burst of particle flux is associated with a burst of zonal flow potential ($k_\theta \rho_i = 0$). The zonal flows are only slowly damped by ion-ion collisions [27]. Once driven to high amplitude, zonal flows suppress the primary modes for many linear growth times. The zonal flows appear to be driven by secondary instability [28, 29] (so-called *modulational instability* when near threshold), for which the zonal flow growth rate is proportional to the exponentially growing amplitude of the primary mode. Once the secondary is triggered, the zonal flow potential ϕ_{ZF} explodes with $\phi_{ZF} \propto \exp(\exp \gamma t)$, where γ is the primary growth rate, and nearly all of the energy present in the primary modes is rapidly transferred to the (slowly damped) zonal flows, shown in Fig. 9(c). For stronger instability drive, the zonal flow bursts become more intermittent, and the zonal flow amplitude competes with the primary mode amplitudes, resulting in intermittent bursts of particle flux, as shown in Fig. 9(d,e).

Finally, we have demonstrated that the nonlinear upshift of the TEM critical density gradient increases with collisionality, which is favorable to higher density. In Fig. 10, the particle flux from pure TEM turbulence is shown as a function of the driving factor, the inverse density gradient scale length. Increasing the collisionality by an order of magnitude does not significantly change the linear TEM threshold, for low collisionality. The increased ion-ion collisions have a relatively weak effect on the zonal flows, but the increased electron-ion collisions strongly
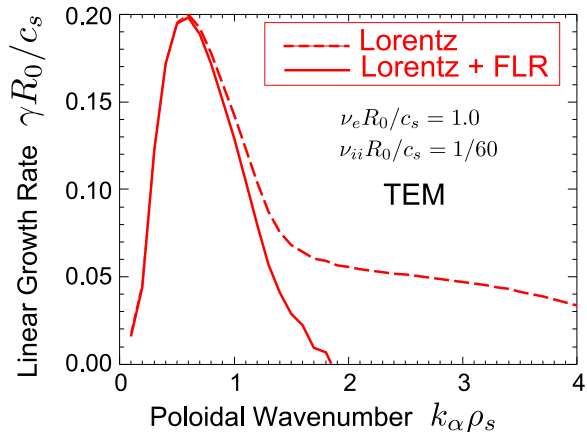
damp TEMs via detrapping. The effect of electron-ion collisions on the trapped-passing boundary layer is proportional to $\{\nu_e/(\varepsilon\omega_{De})\}^{1/2}$ [30].
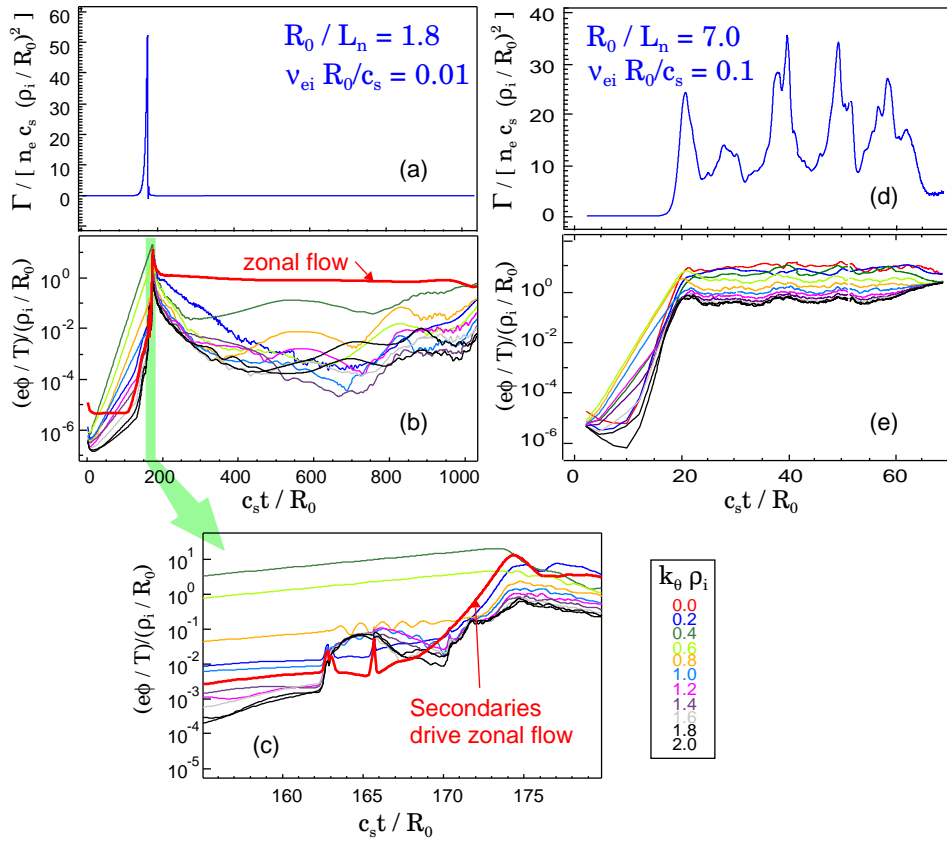

FIG. 9. *Zonal flow dominated states arise near the linear critical density gradient for TEM onset. (a) Particle flux displays single burst, (b) electrostatic potential dominated by weakly damped zonal flow, driven to large amplitude by (c) secondary instability; (d) Flux more intermittent with stronger drive, and (e) zonal flow is less dominant above effective nonlinear threshold.*
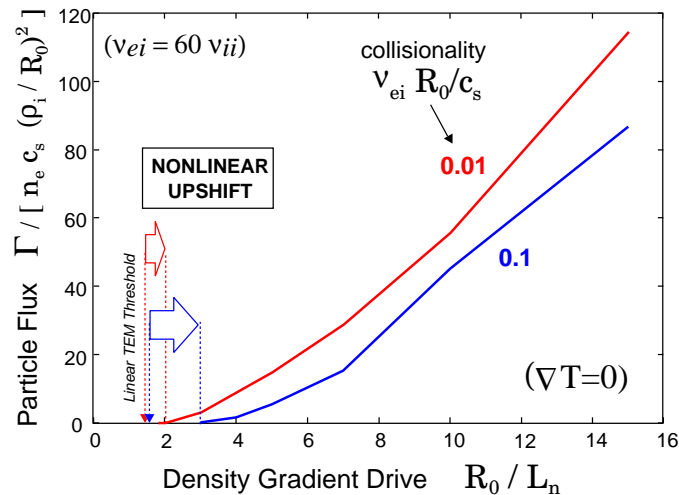

FIG. 10. *Particle flux as function of density gradient for TEM turbulence. Nonlinear upshift increases with collisionality; linear threshold shows weak dependence.*

6. Conclusions

Using a new synthetic Phase Contrast Imaging diagnostic in GS2, nonlinear gyrokinetic simulations reproduce the measured wavelength spectrum of density fluctuations during on-axis heating of the C-Mod ITB. Stability analysis reveals a strong trapped electron mode in the ITB during on-axis heating. Classical ion collisional diffusion is shown to damp shorter wavelength TEMs for realistic collisionalities. The TEM critical gradient displays a nonlinear upshift, associated with the onset of secondary instabilities. The nonlinear upshift increases with collisionality. Finally, more recent PCI measurements can be localized to the upper or lower half of the plasma cross-section, in principle revealing the mode propagation direction. Further, the PCI data reveals significant up-down asymmetry in the wavelength spectra. Such asymmetry could result from sheared rotation or finite ρ_* effects, which will be the subject of future work.

References

[1] ERNST, D. R. et al., Phys. Plasmas **11** (2004) 2637.

[2] ERNST, D. R. et al., in *Proc. 20th IAEA Fusion Energy Conference, Vilamoura, Portugal, 1-6 November 2004*.

[3] WUKITCH, S. J. et al., Phys. Plasmas **9** (2002).

[4] FIORE, C. L. et al., Plasma Phys. Control. Fusion **46** (2004).

[5] FIORE, C. L. et al., Phys. Plasmas **11** (2004) 2480.

[6] RICE, J. E. et al., Nucl. Fusion **41** (2001) 277.

[7] PARKER, S. E. et al., Phys. Rev. Lett. **71** (1993) 2042.

[8] FONCK, R. et al., Phys. Rev. Lett. **70** (1993) 3736.

[9] CANDY, J. et al., Phys. Rev. Lett. **91** (2003) 045001.

[10] DANNERT, T. et al., Phys. Plasmas **12** (2005) 072309.

[11] JENKO, F. et al., Plasma Phys. Contr. Fusion **47** (2005) B195.

[12] MAZURENKO, A. et al., Phys. Rev. Lett. **89** (2002) 225004.

[13] BONOLI, P. T. et al., Bull. Am. Phys. Soc. **46** (2001) 54.

[14] MARMAR, E. et al., Rev. Sci. Instrum. **72** (2001) 940.

[15] PORKOLAB, M. et al., IEEE Transactions in Plasma Science **34** (2006) 229.

[16] DORLAND, W. D. et al., Phys. Rev. Lett. **85** (2000) 5579.

[17] KOTSCHENREUTHER, M. et al., Comp. Phys. Comm. **88** (1995) 128.

[18] ERNST, D. R. et al., Phys. Plasmas **7** (2000) 615.

[19] LONG, A., and ERNST, D. R., Bull. Am. Phys. Soc. **50** (2005) 153, GP1.48.

[20] MILLER, R. L. et al., Phys. Plasmas **2** (1995) 3676.

[21] ROSS, D. W. et al., Phys. Fluids **20** (1977) 613.

[22] CATTO, P. J. et al., Phys. Fluids **20** (1977) 396.

[23] DIMITS, A. M. et al., Phys. Plasmas **7** (2000) 969.

[24] ROACH, C. et al., Plasma Phys. Contr. Fusion **47** (2005) B323.

[25] NAVKAL, V., ERNST, D. R., and DORLAND, W., Bull. Am. Phys. Soc. (2006), 48th Annual Meeting of the Division of Plasma Physics, October 30 - November 3, 2006, Philadelphia, PA, USA, JP1.00017.

[26] ZELLER, K., 2006, Senior thesis, Dept. of Nuclear Science and Engineering, Mass. Inst. of Technology, Cambridge, Massachusetts, USA.

[27] HINTON, F. L. et al., Plasma Phys. Controlled Fusion **41** (1999) A653.

[28] ROGERS, B. N. et al., Phys. Rev. Lett. **85** (2000) 5336.

[29] DIAMOND, P. H. et al., Plasma Phys. Contr. Fusion **47** (2005) R35.

[30] CONNOR, J. W. et al., Plasma Phys. Contr. Fusion **48** (2006) 885.